Nano Research

Open Access

Research Article

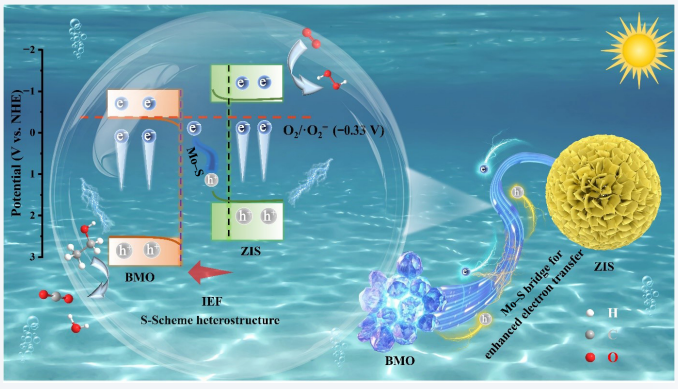
Mo–S bridged $ZnIn_2S_4/Bi_2MoO_6$ S-scheme heterojunction photocatalyst for efficient H_2O_2 production

Shuai Zhang[1,§], Tao Sun[1,§], Hui Lu[1], Guanqi Wang[2], Wei Sun[2], Xueying Cheng[2] ✉, Xingjing Zhang[1] ✉, Renquan Guan[3], and Chunbo Liu[2] ✉

[1] *Key Laboratory of Preparation and Application of Environmental Friendly Materials of the Ministry of Education, College of Chemistry, Jilin Normal University, Changchun 130103, China*
[2] *Science and Technology Innovation Center of Jilin Province for Targeted Identification and Photocatalytic Degradation Materials, College of Engineering, Jilin Normal University, Siping 136000, China*
[3] *State Key Laboratory of Semiconductor Physics and Chip Technologies, Institute of Semiconductors, Chinese Academy of Sciences, Beijing 100083, China*
§ *Shuai Zhang and Tao Sun contributed equally to this work.*

Cite this article: *Nano Research*, **2026**, *19*, 94908930. https://doi.org/10.26599/NR.2026.94908930

ABSTRACT: Sulfide-based photocatalysts hold promise for visible-light-driven H_2O_2 synthesis; however, the low efficiency of photogenerated charge carrier separation and migration remains a critical bottleneck limiting their overall yield. In response to this challenge, the construction of S-scheme heterojunctions represents a promising strategy to expedite charge carrier migration, enhance charge utilization, and consequently boost photocatalytic H_2O_2 production. This study successfully prepared an S-scheme $ZnIn_2S_4/Bi_2MoO_6$ heterojunction photocatalyst, bridged by interfacial Mo–S bonds, via a hydrothermal method. This catalyst achieved a high production rate of up to 1387 $\mu mol \cdot g^{-1} \cdot h^{-1}$ in the photocatalytic generation of H_2O_2. Combining *in-situ* spectroscopic characterization with density functional theory calculations, it was clarified that the formation of Mo–S bonds induces the construction of the S-scheme heterojunction. The synergistic effect of the interfacial built-in electric field and band alignment drives the spatial separation and directional migration of photogenerated charge carriers, as well as the dynamic evolution of the key oxygen intermediate, thereby enabling the efficient generation of H_2O_2 via the two-electron oxygen reduction reaction pathway. This work provides a novel interfacial engineering strategy and mechanistic insights for designing efficient and stable S-scheme heterojunction catalysts for the green photocatalytic synthesis of H_2O_2.



KEYWORDS: $ZnIn_2S_4/Bi_2MoO_6$, Mo–S bonds, S-scheme, photocatalysis, H_2O_2

1 Introduction

Hydrogen peroxide (H_2O_2), as an important clean energy source, has been widely applied in fields such as wastewater treatment, organic synthesis, and medical disinfection [1–4]. Currently, the large-scale production of H_2O_2 mainly relies on the anthraquinone process and direct synthesis from hydrogen and oxygen; however, these methods suffer from high energy consumption and complex procedures, which limit their application [5, 6]. In contrast, photocatalytic technology harnesses solar energy to drive H_2O_2 synthesis, offering advantages such as green sustainability, mild reaction conditions, and low raw material costs [7, 8]. However, the rapid recombination of photogenerated charge carriers is a critical bottleneck limiting the efficiency of photocatalytic H_2O_2 synthesis [9, 10], necessitating the enhancement of charge separation efficiency through materials design strategies such as interface engineering [11, 12].

$ZnIn_2S_4$ (ZIS), as a typical layered metal sulfide, has garnered

Received: April 15, 2026; **Revised:** June 7, 2026
Accepted: June 13, 2026

✉Address correspondence to Xueying Cheng, chengxy@jlnu.edu.cn; Xingjing Zhang, xjzhang128@163.com; Chunbo Liu, chunboliu@jlnu.edu.cn

widespread attention in photocatalytic H_2O_2 synthesis due to its excellent optical properties, good visible-light absorption capability, and suitable band structure [13, 14]. However, it is confronted with the dual constraints of severe charge carrier recombination and low surface reaction efficiency [15, 16]. Bi_2MoO_6 (BMO) possesses advantages such as a large specific surface area, high chemical stability, and strong metal interactions, but its narrow visible-light absorption range results in insufficient catalytic capability [17–20]. In light of the respective limitations of single photocatalysts, constructing an S-scheme heterojunction based on interfacial chemical bonding has become an effective strategy to enhance photocatalytic performance [21, 22]. Meanwhile, at the atomic scale, interfacial chemical bonds are formed at the ZIS/BMO interface through Mo–S orbital hybridization [23, 24]. This orbital coupling induces a redistribution of interfacial electron density, thereby enhancing the built-in electric field and constructing atomic-level charge transport channels. It further synergizes with the S scheme heterojunction to improve the separation efficiency of photogenerated charge carriers and the interfacial reaction kinetics, ultimately boosting the efficiency of photocatalytic H_2O_2 synthesis [25, 26].

Herein, we successfully constructed an S-scheme ZIS/BMO heterojunction photocatalyst featuring Mo–S bonds as the interfacial bridging linkage via a hydrothermal method. This heterojunction architecture effectively promoted the spatial separation of photogenerated charge carriers, significantly enhanced the efficiency of H_2O_2 production via oxygen reduction, and achieved a high yield of 1387 $\mu mol \cdot g^{-1} \cdot h^{-1}$. Integrated *in-situ* spectroscopy and density functional theory (DFT) calculations revealed that the formation of Mo–S interfacial bonds enabled the construction of the ZIS/BMO S-scheme heterojunction. The synergy between the two components resulted in efficient charge carrier separation and migration, consequently driving highly efficient H_2O_2 production through the $2e^-$ oxygen reduction reaction (ORR) route. This study provides new insights and experimental evidence for the design of efficient and stable heterojunction-based photocatalytic systems for H_2O_2 synthesis.

2 Experimental

2.1 Materials

The ultrapure water (resistivity 18.2 ≥ MΩ·cm) used in the experiments was provided by the HHItech-Ultra system. All chemical reagents were of analytical grade and used as received without further purification. The materials were obtained from commercial suppliers as follows:

Zinc chloride ($ZnCl_2$, 98%), thioacetamide (TAA, 99%), indium(III) chloride tetrahydrate ($InCl_3 \cdot 4H_2O$, 99%), sodium molybdate dihydrate ($Na_2MoO_4 \cdot 2H_2O$, 99.95%), potassium hydrogen phthalate ($C_8H_5KO_4$, 99.8%), p-benzoquinone (p-BQ, 99%), potassium iodide (KI, 99.8%), and sodium sulfate (Na_2SO_4, ≥ 99%) were purchased from Macklin Biochemical Co., Ltd. (Shanghai, China). Absolute ethanol (C_2H_5OH, ≥ 99.7%) was supplied by Tianjin Tianli Chemical Reagent Co., Ltd. Ethylene glycol ($HOCH_2CH_2OH$, ≥ 99.5%) and hydrochloric acid (HCl, 36%–38%) were obtained from Chengdu Kelong Chemical Co., Ltd. Ethylenediaminetetraacetic acid disodium salt (EDTA-2Na, ≥ 98%) was purchased from Shanghai Haohong Biomedical Technology Co., Ltd. Bismuth(III) nitrate pentahydrate ($Bi(NO_3)_3 \cdot 5H_2O$, 99%), silver nitrate ($AgNO_3$, ≥ 99.8%), polyvinylidene fluoride (PVDF), and isopropanol (IPA, > 99%) were purchased from Shanghai Aladdin Biochemical Technology Co., Ltd. Acetylene black (99.5%) was supplied by Shanghai Yien Chemical Technology Co., Ltd. N-Methyl-2-pyrrolidone (C_5H_9NO, ≥ 99%) and hydrogen peroxide (H_2O_2, 30%) were obtained from Sinopharm Chemical Reagent Co., Ltd. (Shanghai, China). Sodium hydroxide (NaOH, ≥ 96%) was purchased from Tianjin Tiantai Chemical Co., Ltd.

2.2 Synthesis of BMO

$Bi(NO_3)_3 \cdot 5H_2O$ (4 mmol, 1.940 g) was dissolved in 40 mL of ethylene glycol (EG), and $Na_2MoO_4 \cdot 2H_2O$ (2 mmol, 0.484 g) was separately dissolved in 10 mL of ethanol, with both solutions stirred rapidly until fully dissolved. Subsequently, the mixed solutions were transferred to a 100 mL Teflon-lined autoclave and hydrothermally treated at 190 °C for 2 h. Upon cooling to room temperature, the precipitate was isolated and sequentially washed three times with deionized water and ethanol by centrifugation. The purified solid was dried under vacuum at 70 °C for 12 h, yielding BMO as the final product.

2.3 Synthesis of ZIS/BMO

Initially, $ZnCl_2$ (1 mmol, 0.136 g), $InCl_3 \cdot 4H_2O$ (2 mmol, 0.587 g), and TAA (2 mmol, 0.15 g) were measured into a 100 mL beaker, after which 70 mL of deionized water was added. The solution was ultrasonicated for 20 min and subsequently magnetically stirred for 30 min to ensure complete dissolution. Subsequently, varying amounts of BMO (0, 0.025, 0.12, 0.24, and 0.36 mmol) were added to the beaker, and the mixture was stirred for an additional 30 min. The well-mixed solution was then transferred into a 100 mL Teflon-lined autoclave and heated at 160 °C for 20 h. Upon cooling to ambient temperature, the precipitate was centrifugally washed three times sequentially with deionized water and ethanol. The final products were dried under vacuum at 60 °C for 12 h, yielding catalysts with varying BMO compositions, designated as ZIS, ZIS/BMO 1%, ZIS/BMO 5%, ZIS/BMO 10%, and ZIS/BMO 15% (Fig. 1(a)). Among them, the sample ZIS/BMO 5% was named as ZIS/BMO.

2.4 Performance measurement

Photocatalytic H_2O_2 generation tests were conducted using a multi-channel parallel photoreactor (PCX 50 C, Beijing Perfect Light, China). First, 10 mg of ZIS/BMO catalyst was uniformly dispersed in 50 mL of 10% aqueous ethanol solution. Then, oxygen was continuously purged into the solution under dark conditions with stirring for 30 min, after which the mixture was exposed to visible light (10 W light-emitting diode (LED), 100 $mW \cdot cm^{-2}$, λ = 400–800 nm) for 30 min. Every 5 min, 2 mL of the reaction solution was sampled, filtered through a 0.45 μm membrane filter, and subjected to iodometric titration by mixing 1 mL filtrate with 2 mL of an equal-volume mixture of potassium hydrogen phthalate (0.1 $mol \cdot L^{-1}$) and KI (0.4 $mol \cdot L^{-1}$). Ultraviolet–visible (UV–vis) spectrophotometry (350 nm) was employed to determine H_2O_2 concentration. Furthermore, IPA, p-BQ, EDTA-2Na, and $AgNO_3$ were employed as scavengers for hydroxyl radicals (·OH), superoxide radicals (O_2^-), holes (h^+), and electrons (e^-), respectively, to probe the primary active species. The photocatalytic H_2O_2 degradation experiment was performed by dispersing 10 mg catalyst in 50 mL of 1 $mmol \cdot L^{-1}$ H_2O_2 aqueous solution under N_2 purging with 30 min light irradiation.

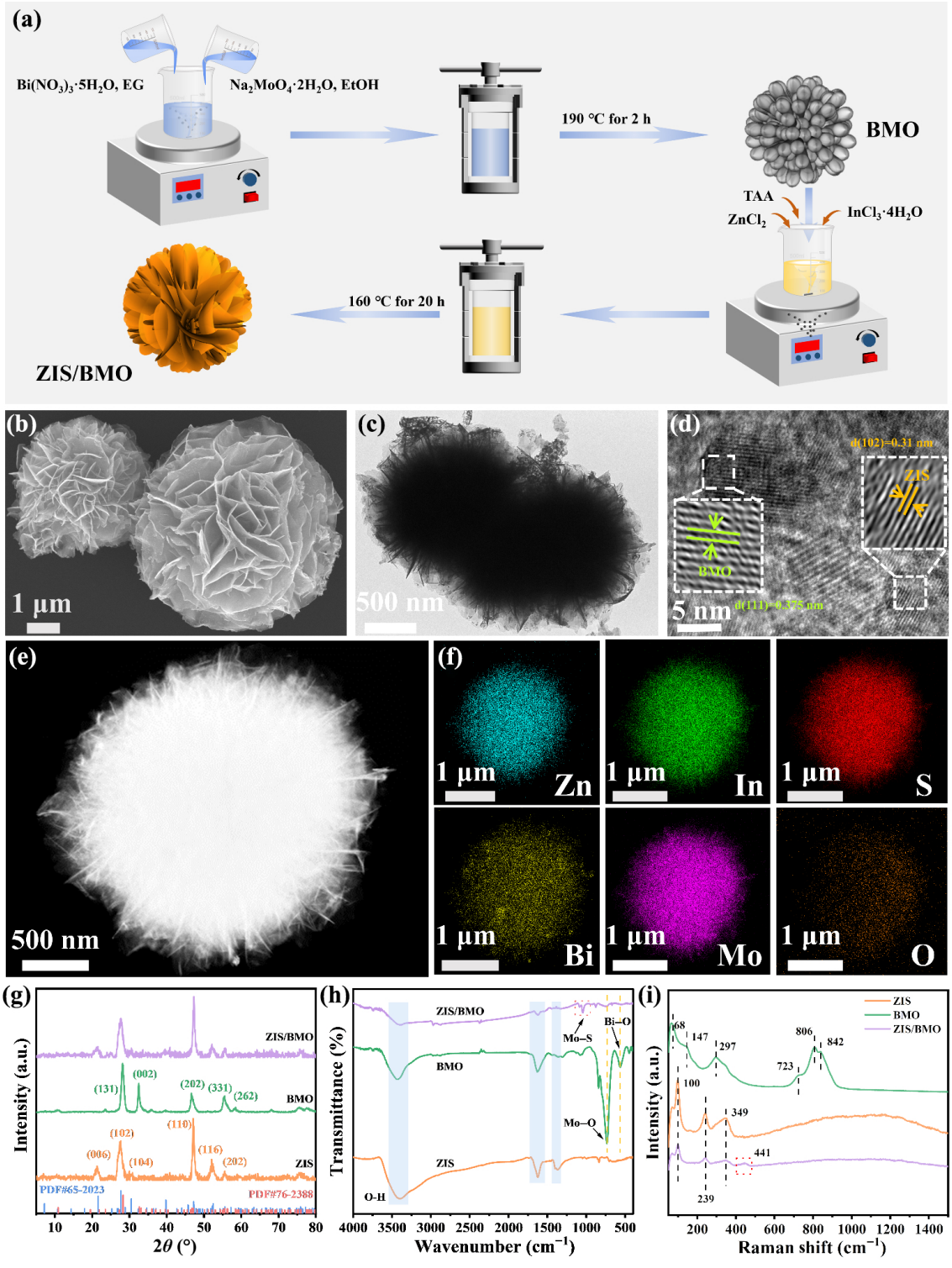


Figure 1 Schematic diagram of the ZIS/BMO hetero-junction formation route (a). SEM images of ZIS/BMO (b). TEM (c), HRTEM (d), HAADF-STEM images and corresponding elemental distributions (e) and (f), XRD (g), FT-IR (h), and Raman (i) of ZIS, BMO, and ZIS/BMO.

3 Results and discussion

3.1 Mo–S bridged $ZnIn_2S_4/Bi_2MoO_6$ S-Scheme heterojunction

The morphology of the synthesized photocatalysts was characterized by scanning electron microscopy (SEM) and transmission electron microscopy (TEM). Figure S1(a) in the Electronic Supplementary Material (ESM) displays the spherical ZIS nanoflower architecture, which is composed of assembled nanosheets [27]. Figure S1(b) in the ESM illustrates the spherical morphology of the BMO sample [28]. Compared to pure ZIS, the SEM image of the ZIS/BMO composite reveals a more uniform and well-defined nanoflower spherical structure (Fig. 1(b)). These

observations suggest that the BMO substrate is encapsulated within the ZIS nanosheets, and the interfacial interactions guide the assembly process of the ZIS nanosheets, promoting the formation of a highly ordered hierarchical architecture. The TEM image of ZIS/BMO shown in Fig. 1(c) further demonstrates the combination of ZIS on the BMO surface [29]. From the high-resolution transmission electron microscopy (HR-TEM) image of ZIS/BMO (Fig. 1(d)), lattice fringe spacings of 0.31 and 0.375 nm are observed, corresponding to the (102) plane of ZIS and the (111) plane of BMO, respectively [28, 30]. Figures 1(e) and 1(f) show the elemental distribution of ZIS/BMO in the high-angle annular dark-field (HAADF) mode. The elements Zn, In, S, Bi, Mo, and O are uniformly distributed across the sample surface, confirming the successful combination of the two components.

The crystal structure of the catalysts was characterized by X-ray diffraction (XRD) (Fig. 1(g)). The diffraction peaks of ZIS are located at 21.4°, 27.7°, 30.5°, 47.1°, 52.1°, and 55.7°, corresponding to the (006), (102), (104), (110), (116), and (202) crystal planes, respectively, which are consistent with the PDF#65-2023 standard card [31]. The diffraction peaks of BMO are located at 28.1°, 32.4°, 46.6°, 55.5°, and 58.5°, corresponding to the (131), (002), (202), (331), and (262) crystal planes, respectively, matching the PDF#76-2388 standard [32]. No obvious BMO diffraction peaks were observed in the ZIS/BMO, which is attributed to the encapsulation of BMO by ZIS nanosheets and its low content. As the BMO content increased, its characteristic diffraction peaks gradually appeared (Fig. S2 in the ESM), confirming the successful integration of ZIS and BMO [33].

The molecular vibration characteristics and interfacial chemical bonding mechanisms of the samples were analyzed by Fourier transform infrared (FT-IR) spectroscopy (Fig. 1(h)). The broad absorption peak at 3400 cm^{-1} is assigned to the O–H stretching vibration of surface-adsorbed water, while the peaks at 1620 and 1370 cm^{-1} correspond to the H–O–H bending vibrations of H_2O [34]. The absorption band observed for ZIS between 500 and 650 cm^{-1} is assigned to the Zn–S and In–S stretching vibrations. The characteristic peaks of BMO at 732 and 556 cm^{-1} are assigned to the Mo–O and Bi–O stretching vibrations, respectively [35]. The retention of the characteristic vibration peaks of both components in ZIS/BMO confirms the successful combination of ZIS and BMO. Notably, the newly emerged absorption peak at 1051 cm^{-1} can be assigned to the Mo–S bond stretching vibration, indicating the formation of a chemically bonded heterointerface between ZIS and BMO via Mo–S bridging [36].

The molecular structure and vibration modes obtained from Raman spectroscopy provide direct evidence for the formation of interfacial chemical bonds in ZIS/BMO (Fig. 1(i)). The Raman spectrum of BMO exhibits characteristic vibration peaks at 68, 147, 806, 842, and 297 cm^{-1} [37], while ZIS shows characteristic peaks at 100, 239, and 349 cm^{-1} [38]. Notably, no distinct BMO characteristic peaks are observed in the Raman spectrum of ZIS/BMO, which is attributed to the low crystallinity and relatively low content of BMO. Additionally, a new vibration peak appears at 441 cm^{-1}, which, combined with the FT-IR analysis, can be assigned to the vibrational mode of Mo–S bonds, providing direct evidence for the formation of a chemically bridged interfacial structure between ZIS and BMO via Mo–S bonds [36]. These results demonstrate that Mo–S bonds serve as interfacial chemical bridges, effectively connecting ZIS and BMO and establishing a structural foundation for constructing a stable heterointerface and promoting interfacial transport of photogenerated charge carriers.

N_2 adsorption–desorption measurements were conducted to systematically study the specific surface areas and pore structures of ZIS, BMO, and ZIS/BMO. As presented in Figs. S3(a) and S3(b) in the ESM, the adsorption–desorption isotherms for all three samples display characteristic Type-IV profiles accompanied by H3-type hysteresis loops (based on IUPAC classification), demonstrating the mesoporous nature of ZIS/BMO. It is noteworthy that upon incorporation of BMO, the specific surface area of ZIS/BMO (83 $m^2 \cdot g^{-1}$) shows a further enhancement relative to pure-phase ZIS (70 $m^2 \cdot g^{-1}$) (Table S1 in the ESM). This phenomenon can be attributed to the role of BMO as a substrate, which effectively facilitates the uniform growth of ZIS nanosheets and inhibits nanoparticle aggregation. This provides more active sites for the photocatalytic reaction, which is conducive to the adsorption and transport of reactant molecules [39]. Based on the thermogravimetric analysis (TGA) results (Fig. S4(a) in the ESM), O_2 temperature-programmed desorption (O_2-TPD) measurements were conducted (Fig. S4(b) in the ESM). Comparison of the peak areas reveals that the O_2 adsorption amounts of BMO and ZIS/BMO are roughly comparable, whereas that of ZIS is significantly weaker. Regarding the desorption peak positions, ZIS shows a peak at 331 °C, BMO at 391 °C, and ZIS/BMO exhibits an additional new peak at a higher temperature of 691 °C besides its peak at 452 °C. This indicates that ZIS/BMO possesses a stronger O_2 adsorption capability [40].

3.2 Band structure and internal electric field-enhanced charge transfer kinetics of ZIS/BMO

The optical absorption characteristics of the catalysts were examined by UV–visible diffuse reflectance spectroscopy (UV–vis DRS) (Fig. S5 in the ESM). As depicted in Fig. 2(a), ZIS displays an absorption edge at about 628 nm, and BMO shows an absorption edge near 480 nm. Compared to ZIS, the absorption edge of ZIS/BMO exhibits a red shift, confirming the enhanced light-harvesting capability of ZIS/BMO. Furthermore, the Tauc plots of the prepared samples were obtained using the Kubelka–Munk function (Fig. 2(b)), showing that the band gap (E_g) values of ZIS and BMO are 2.46 and 2.90 eV, respectively. Furthermore, the flat-band potentials (V_{fb}) of the samples were determined using Mott–Schottky (M–S) measurements at different frequencies (1000, 1500, and 2000 Hz). The M–S plots of both ZIS and BMO exhibit positive slopes, indicating that they are typical n-type semiconductors (Fig. 2(c)). The V_{fb} potentials of ZIS and BMO were determined to be −0.93 and −0.43 eV, respectively. The potential was converted to the normal hydrogen electrode (NHE) scale using the Nernst equation: E (NHE) = E (Ag/AgCl) + 0.197. For an n-type semiconductor, the conduction band (CB) edge is typically about 0.1 V more negative than the flat-band potential (V_{fb}) [41]. Accordingly, the conduction band potentials of ZIS and BMO were determined to be −0.83 and −0.33 V, respectively. In summary, the band structure of ZIS/BMO is depicted in Fig. 2(d). It is noteworthy that the band alignment of ZIS/BMO not only meets the thermodynamic requirements for ORR but also satisfies the prerequisite for forming an S-scheme heterojunction.

The chemical states of ZIS, BMO, and ZIS/BMO were systematically analyzed by X-ray photoelectron spectroscopy (XPS) (Figs. S6 and S7 in the ESM). In the Zn 2p spectrum of ZIS (Fig. S7(a) in the ESM), the characteristic peaks for pure ZIS corresponding to Zn $2p_{1/2}$ and Zn $2p_{3/2}$ are located at 1045.2 and 1022.2 eV, respectively [42]. For ZIS/BMO, these two peaks shift

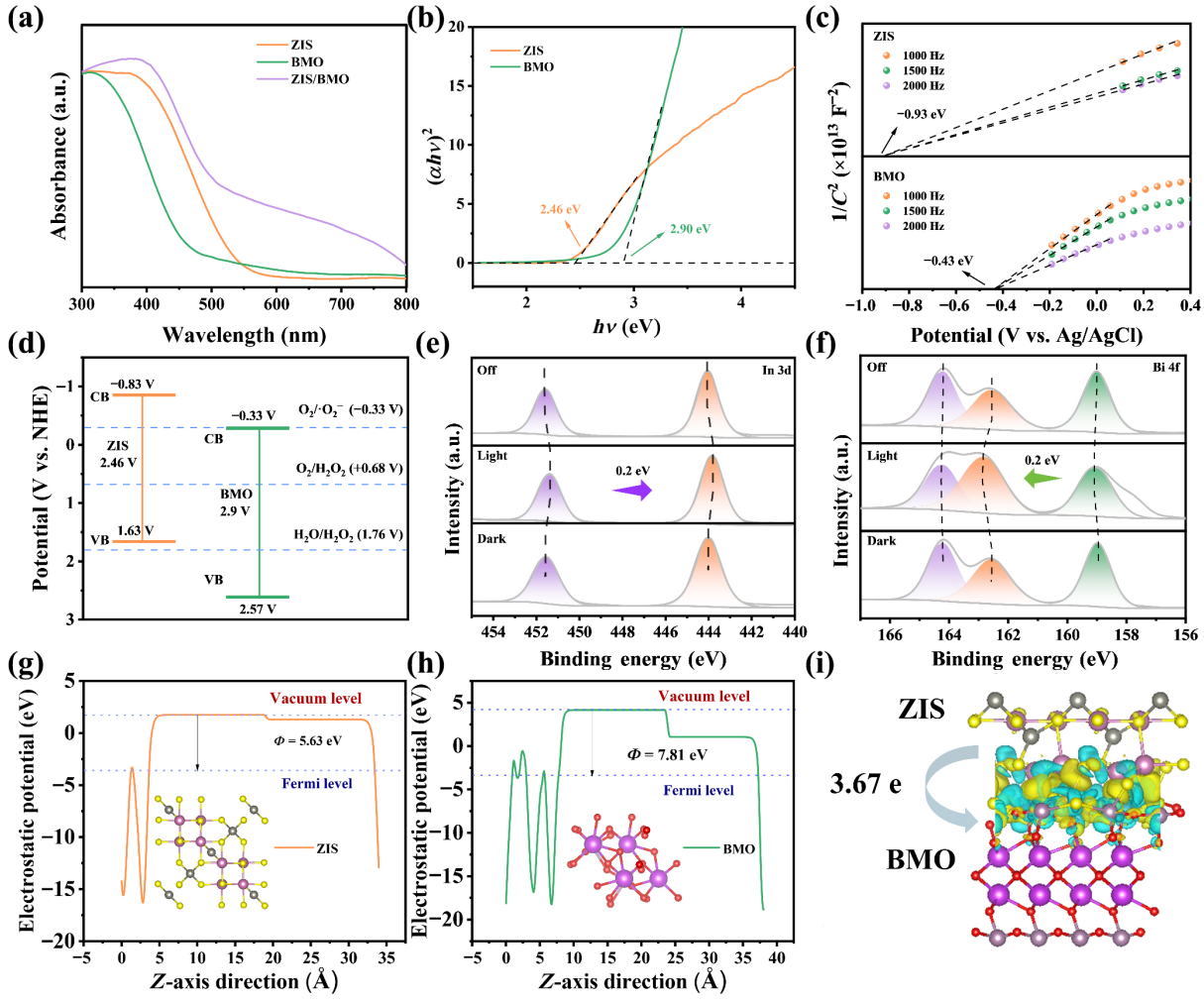


Figure 2 UV–vis DRS of ZIS, BMO and ZIS/BMO (a), corresponding Tauc plots (b), Mott–Schottky plots (c) of ZIS and BMO, the calculated band structures (d), *in-situ* XPS In 3d (e) and Bi 4f (f), calculated work functions for ZIS (g) and BMO (h), differential charge density bader charge analysis of ZIS/BMO (i).

positively to 1045.6 and 1022.4 eV, respectively. Similarly, in the high-resolution In 3d spectrum (Fig. S7(b) in the ESM), two characteristic peaks appear at 445.0 and 452.5 eV, corresponding to the In $3d_{5/2}$ and In $3d_{3/2}$ orbitals, respectively, which is consistent with the chemical state of In^{3+} [43]. For the ZIS/BMO, these characteristic peaks shift to 445.3 and 452.8 eV, indicating a positive binding energy shift of 0.3 eV. The S 2p spectrum (Fig. S7(c) in the ESM) reveals that the characteristic peaks of ZIS (S $2p_{3/2}$ at 163 eV and S $2p_{1/2}$ at 161.8 eV) shift to higher binding energies upon forming the composite with BMO [44]. These results demonstrate that upon incorporation of BMO, the binding energies of the constituent elements in ZIS increase, implying a loss of electrons from ZIS. Analysis of the Bi 4f orbitals (Fig. S7(d) in the ESM) shows that BMO displays two prominent peaks at 158.7 and 164.1 eV, attributed to Bi $4f_{7/2}$ and Bi $4f_{5/2}$, respectively, confirming the presence of Bi in the +3 oxidation state [45]. In ZIS/BMO, besides the aforementioned characteristic peaks, a new peak appears at 161.7 eV. This is due to the overlap between the characteristic binding energy range of the S 2p orbital (161–163 eV) and the Bi 4f spectral region; this new peak is likely contributed by the S 2p orbital. This provides further indication of potential interfacial interactions between ZIS and BMO. In the Mo 3d spectrum (Fig. S7(e) in the ESM), the characteristic peaks of BMO for Mo $3d_{3/2}$ (235.5 eV) and Mo $3d_{5/2}$ (232.3 eV) also show a shift to lower binding energies upon forming the composite with ZIS [46]. It is noteworthy that in the O 1s spectrum of BMO (Fig. S7(f) in the ESM), the characteristic peaks located at 530.2 and 529.2 eV are assigned to the Mo–O and Bi–O bonds, respectively. In the ZIS/BMO, these peaks shift to higher binding energies, a trend opposite to that observed for the Mo 3d and Bi 4f orbitals. This may be due to the interfacial interactions at the heterojunction enhancing the coupling between BMO and ZIS, consequently leading to an increase in the O 1s orbital binding energy [47]. The observed binding energy shifts indicate strong electronic interactions between ZIS and BMO, with electron transfer occurring from ZIS to BMO at the interface. *In-situ* XPS characterization was performed to further confirm the existence of an electronic coupling effect between ZIS and BMO. The direction of electron transfer was identified by comparing the XPS spectra acquired under light irradiation. The binding energy of the In 3d characteristic peaks in ZIS/BMO shows a negative shift under light illumination, indicating that ZIS gains electrons during this process (Fig. 2(e)). In contrast, a positive shift in the characteristic peaks of the Bi 4f and O 1s orbitals for ZIS/BMO under light irradiation (Fig. 2(f)) verifies the loss of electrons from BMO. These results elucidate the strong interaction between ZIS and BMO under

in-situ light exposure and the process of photogenerated electron transfer from BMO to ZIS (Fig. S8 in the ESM).

To elucidate the interfacial charge transfer mechanism in ZIS/BMO in detail, the electronic structure characteristics were systematically examined by ultraviolet photoelectron spectroscopy (UPS) (Fig. S9 in the ESM). The work functions for ZIS, BMO, and ZIS/BMO were determined to be 3.67, 4.12, and 3.89 eV, respectively [48]. Consequently, upon contact, electrons spontaneously transfer from the higher Fermi level (ZIS) to the lower Fermi level (BMO) until the Fermi levels equilibrate. This finding is in agreement with the elemental binding energy shifts observed in XPS analysis. For a more in-depth investigation of the electronic structure, we performed work function calculations using DFT. The work function (Φ) is crucial for evaluating the Fermi level position and elucidating the charge carrier transfer between ZIS and BMO, as it estimates the energy difference between the vacuum level and the Fermi level [49]. As depicted in Figs. 2(g) and 2(h), the calculated work functions for BMO and ZIS are 7.81 and 5.63 eV, respectively. A lower work function implies a higher Fermi level, indicating that ZIS possesses a higher Fermi level compared to BMO. This suggests that after the introduction of BMO, photogenerated electrons preferentially transfer from ZIS to BMO. This conclusion is consistent with the results obtained from UPS and XPS. Further validation of the interfacial charge transfer was achieved through Bader charge analysis (Fig. 2(i)). The results reveal the accumulation of positive charge on the ZIS surface and negative charge on the BMO surface at the interface, demonstrating electron transfer from ZIS to BMO. This charge transfer direction aligns with the aforementioned XPS results and provides direct evidence for the establishment of an IEF, serving as a key driving force for the effective separation and transport of photogenerated carriers [50].

To conclude, the S-scheme charge transfer mechanism provides a rational explanation for the superior photocatalytic H_2O_2 production activity observed in the ZIS/BMO material. The electronic band alignment, established according to the work function discrepancy, unambiguously illustrates the charge separation route at the interface (Fig. S10 in the ESM). Before contact, the Fermi level of ZIS is higher than that of BMO, exhibiting a significant energy level difference. Upon contact and equilibration, an internal electric field (IEF) oriented from ZIS towards BMO is established at the heterojunction interface. This results in upward band bending for ZIS and downward band bending for BMO, facilitating the transfer of photogenerated electrons to the ZIS conduction band and the concentration of holes in the BMO valence band. A common Fermi level is finally achieved, leading to the formation of a stable charge transport pathway across the interface. In this process, a portion of the photogenerated electrons from the BMO conduction band recombines with holes residing in the ZIS valence band, propelled by the combined action of the IEF and the band bending. Meanwhile, the electrons in the conduction band of ZIS and the holes in the valence band of BMO are effectively preserved. This S-scheme charge transfer route effectively removes the less useful electrons (originating from the BMO CB) possessing inferior reducing power and the less potent holes (from the ZIS VB) with weaker oxidizing power, while preserving the highly active charge carriers (electrons in the ZIS CB and holes in the BMO VB) that exhibit strong redox abilities. The formation of the S-scheme heterojunction facilitates not only the effective spatial separation and directed transport of photogenerated carriers, but also imparts the ZIS/BMO with enhanced redox potentials, consequently leading to a remarkable improvement in the photocatalytic H_2O_2 production efficiency.

3.3 S-scheme heterojunction-driven efficient photocatalytic H_2O_2 synthesis performance

Using a solvent system comprising 45 mL deionized water and 5 mL ethanol, the photocatalytic H_2O_2 production performance of composites with varying BMO loading ratios was systematically assessed. Figure 3(a) shows that BMO alone demonstrates low photocatalytic activity, producing only trace amounts of H_2O_2, which is attributed to the fast recombination of its photogenerated charge carriers [51]. Conversely, the ZIS/BMO material shows markedly enhanced photocatalytic activity, with an H_2O_2 yield reaching 1387 $\mu mol \cdot g^{-1} \cdot h^{-1}$ (Fig. 3(b)), approximately double that of pristine ZIS. This enhancement is attributed to the accelerated migration of photogenerated electrons and improved charge carrier separation efficiency after introducing BMO, where the strong interfacial interaction between the two components is essential for efficient photocatalytic H_2O_2 production. Furthermore, when the BMO loading exceeds 10 wt.%, the catalytic performance shows a declining trend. This is because excessive BMO leads to a light-shielding effect, which reduces photon absorption efficiency and impedes interfacial charge migration [52]. This result is consistent with the DRS measurement of the samples. Considering the concurrent decomposition of H_2O_2 during photocatalytic synthesis, the H_2O_2 decomposition behavior of the materials was further examined in a N_2 atmosphere (Fig. S11 in the ESM). The formation rate constant (K_f) and decomposition rate constant (K_d) rate constants of the generated H_2O_2 were estimated using zero-order and first-order kinetics models, respectively. The K_f and K_d values for ZIS, BMO, and ZIS/BMO were determined by fitting the photocatalytic H_2O_2 formation data obtained within 30 min (Fig. 3(a)). According to the fitting results, ZIS/BMO possesses a significantly higher K_f value (Fig. 3(c)), demonstrating its superior performance in photocatalytic H_2O_2 production. Additionally, the ZIS/BMO exhibits good stability over five consecutive reaction cycles, with the H_2O_2 production rate decreasing by only 23.2% (Fig. 3(d)), which is mainly attributable to catalyst loss during recycling. Concurrently, the structural and catalytic stability of ZIS/BMO was further corroborated by post-reaction characterization using XRD, SEM imaging, and XPS (Figs. S12–S14 in the ESM).

Photocatalytic hydrogen peroxide production entails a complex series of consecutive reactions, principally comprising the ORR and the water oxidation reaction (WOR). To identify the primary active species involved in the photocatalytic production of H_2O_2, radical trapping experiments were first conducted (Fig. 3(e)). After adding $AgNO_3$ to the reaction environment to scavenge electrons, almost no H_2O_2 production activity was observed for ZIS/BMO, indicating that photogenerated electrons play a crucial role in H_2O_2 formation. Upon the addition of p-BQ, the H_2O_2 production performance of ZIS/BMO decreased by 68%, suggesting that $\cdot O_2^-$ is an important intermediate in the H_2O_2 generation process. Furthermore, after introducing EDTA-2Na as a scavenger for h^+, the H_2O_2 production yield of ZIS/BMO increased. This phenomenon is ascribed to the improved charge separation efficiency resulting from hole consumption, which facilitates the ORR both thermodynamically and kinetically [53]. When IPA was introduced as a quencher for

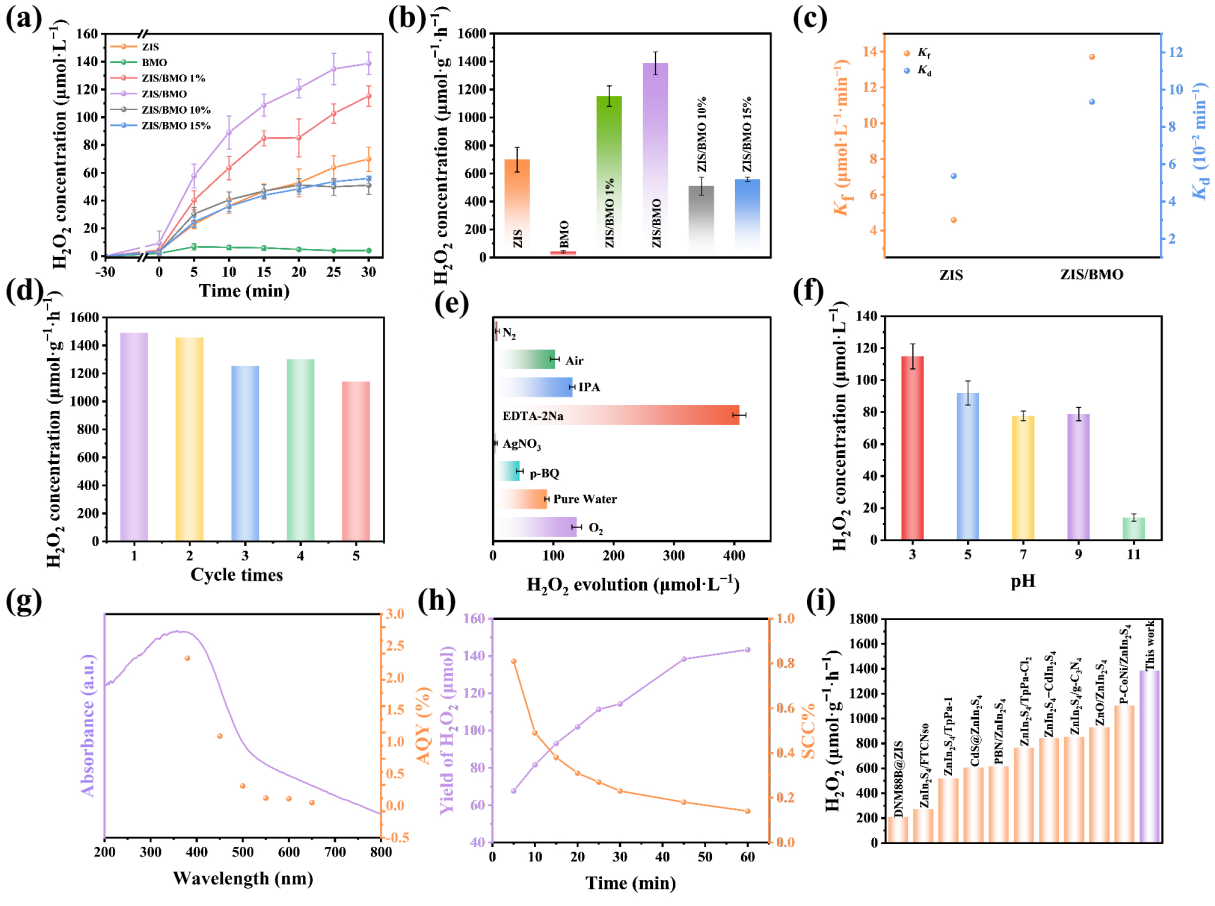


Figure 3 Photocatalytic generation of H_2O_2 of samples under light irradiation (a), comparison of the H_2O_2 evolution amount of samples under light irradiation (b), K_f and K_d of H_2O_2 (c), cycling experiments on ZIS/BMO catalyst (d), comparison of H_2O_2 evolution catalyzed by ZIS/BMO under different conditions (e), photocatalytic yield of H_2O_2 under different pH conditions (f), AQY of H_2O_2 photosynthesis over ZIS/BMO (g), changes in the amounts of H_2O_2 generated and SCC efficiency on ZIS/BMO (h), and photocatalytic H_2O_2 production rates obtained by ZIS/BMO compared with previously reported ZIS-based photocatalysts (i).

·OH, the H_2O_2 yield slightly decreased, implying that a portion of H_2O_2 is generated through the coupling of ·OH radicals. Notably, ZIS/BMO exhibited a considerable H_2O_2 production rate (926.7 μmol·g^{-1}·h^{-1}) even in pure water without any organic scavenger. To evaluate the role of O_2 in the reaction system, H_2O_2 production performance tests were conducted under different atmospheres. Under an air atmosphere, the concentration of H_2O_2 generated by ZIS/BMO was slightly lower than that under an O_2 atmosphere. In contrast, under a N_2 atmosphere, almost no H_2O_2 was produced, indicating that O_2 is a critical factor for H_2O_2 generation, and the ORR primarily governs the production yield of H_2O_2 in the ZIS/BMO photocatalytic system [54]. Furthermore, although its band structure meets the thermodynamic requirements for water oxidation, the lack of efficient active sites for water oxidation results in significant kinetic inhibition of the reaction, thus preventing effective H_2O_2 production [55]. Based on these results, it can be concluded that e^- and $\cdot O_2^-$ are primarily involved in the two-step, single-electron ORR pathway for H_2O_2 production.

Additionally, the influence of pH value and catalyst loading amount on the H_2O_2 production was examined. The ZIS/BMO achieved its maximum yield at pH = 3, with a subsequent decline in H_2O_2 production observed with increasing pH (Fig. 3(f)). This pH dependence originates from the role of protons (H^+) in the photocatalytic ORR; the availability of H^+ decreases under alkaline conditions, leading to a reduction in H_2O_2 concentration [56]. Furthermore, the catalyst dosage experiment results indicate that (Fig. S15 in the ESM) the H_2O_2 production concentration approached saturation upon increasing the ZIS/BMO dosage to 30 mg. This saturation behavior is attributed to the light-shielding effect induced by an excessive amount of catalyst [57].

To demonstrate the correlation between the H_2O_2 production rate and the absorption spectrum of ZIS/BMO, and to confirm the induction of ORR by light, the apparent quantum yield (AQY) of ZIS/BMO was measured under monochromatic light irradiation at different wavelengths (Fig. 3(g)). The variation trend of H_2O_2 yield at different wavelengths was consistent with that of the photo responsive capability. The strong correlation between them confirms the importance of light absorption in the photocatalytic reaction. Meanwhile, under AM 1.5G illumination, the measured solar-to-chemical conversion (SCC) efficiency of ZIS/BMO under visible light irradiation (0.81%) was found to be higher than the solar-to-biomass conversion efficiency of plants (~ 0.1%) (Fig. 3(h)) [58]. This confirms that ZIS/BMO can effectively convert solar energy into releasable chemical energy to drive chemical reactions. Furthermore, the H_2O_2 evolution rate and capacity of ZIS/BMO via photocatalysis are superior to those of most previously reported photocatalysts (Fig. 3(i) and Table S2 in the ESM).

3.4 Enhanced charge separation for efficient 2e$^-$ ORR

The efficiency of charge carrier separation and migration plays a

critical role in determining photocatalytic performance. Initially, the transient photocurrent responses of ZIS, BMO, and ZIS/BMO samples across multiple cycles were measured to evaluate their electron-related photocatalytic activity. Figure 4(a) demonstrates that the ZIS/BMO achieved the maximum photocurrent density, revealing enhanced efficiency in photogenerated carrier transport. Electrochemical impedance spectroscopy (EIS) results showed that, compared to the individual ZIS and BMO samples, ZIS/BMO had the smallest arc radius in the Nyquist plot, indicating reduced interfacial charge transfer resistance and the highest exciton transport efficiency (Fig. 4(b)). Cyclic voltammetry (CV) results show that, compared to ZIS, ZIS/BMO possesses the largest electrochemically active surface area (ECSA), indicating its strongest electron transfer capability (Fig. S16 in the ESM). Furthermore, steady-state photoluminescence (PL) spectra under 380 nm excitation showed the most significant fluorescence quenching for ZIS/BMO, indicating that the formation of the heterojunction suppressed the recombination of photoinduced electron-hole pairs, allowing more electrons to participate in the photocatalytic reaction (Fig. 4(c)). The carrier dynamics of ZIS/BMO were further investigated using time-resolved photoluminescence (TR-PL) spectroscopy (Fig. 4(d)). The average lifetimes of ZIS and BMO were 2.66 and 1.95 ns, respectively, while that of ZIS/BMO increased to 5.56 ns, indicating effective promotion of photogenerated electron-hole separation (Table S3 in the ESM).

Additionally, the DOS of ZIS, BMO, and the ZIS/BMO composite were computed. Figure 4(e) shows that the pristine ZIS and BMO materials both display clear band gaps, verifying their semiconductor properties. In contrast, the density of electronic states near the Fermi level is significantly enhanced in ZIS/BMO, while the bandgap width is markedly reduced. This result indicates a strong electronic synergistic effect between ZIS and BMO, leading to an increased number of unpaired electrons at the Fermi level, which fundamentally enhances the material's conductivity and electron transfer capability [59]. Zeta potential measurements disclosed that ZIS and BMO possess surface potentials of −136.18 and +30.75 mV, respectively, at pH = 3. This opposite zeta potential facilitates the combination of the two materials (Fig. 4(f)). Efficient charge separation and migration facilitate the generation of high surface charge density, thereby promoting redox reactions on the catalyst surface. The zeta potential of ZIS/BMO showed a further negative shift to −382.34 mV, signifying an increased surface charge density. This enhances the interfacial interaction with H^+, thereby establishing favorable conditions for the proton-assisted oxygen reduction pathway, and consequently boosts the photocatalytic H_2O_2 production yield. This result is consistent with the optimal performance of ZIS/BMO at pH = 3 [60, 61].

The thickness of the samples before and after the combination of ZIS and BMO was investigated using atomic force microscopy (AFM) (Figs. S17(a)–S17(d) in the ESM), which demonstrated the assembly mode of ZIS and BMO combination. Furthermore, the thinner the structure, the larger its effective specific surface area, thereby exposing more active sites, which is beneficial for

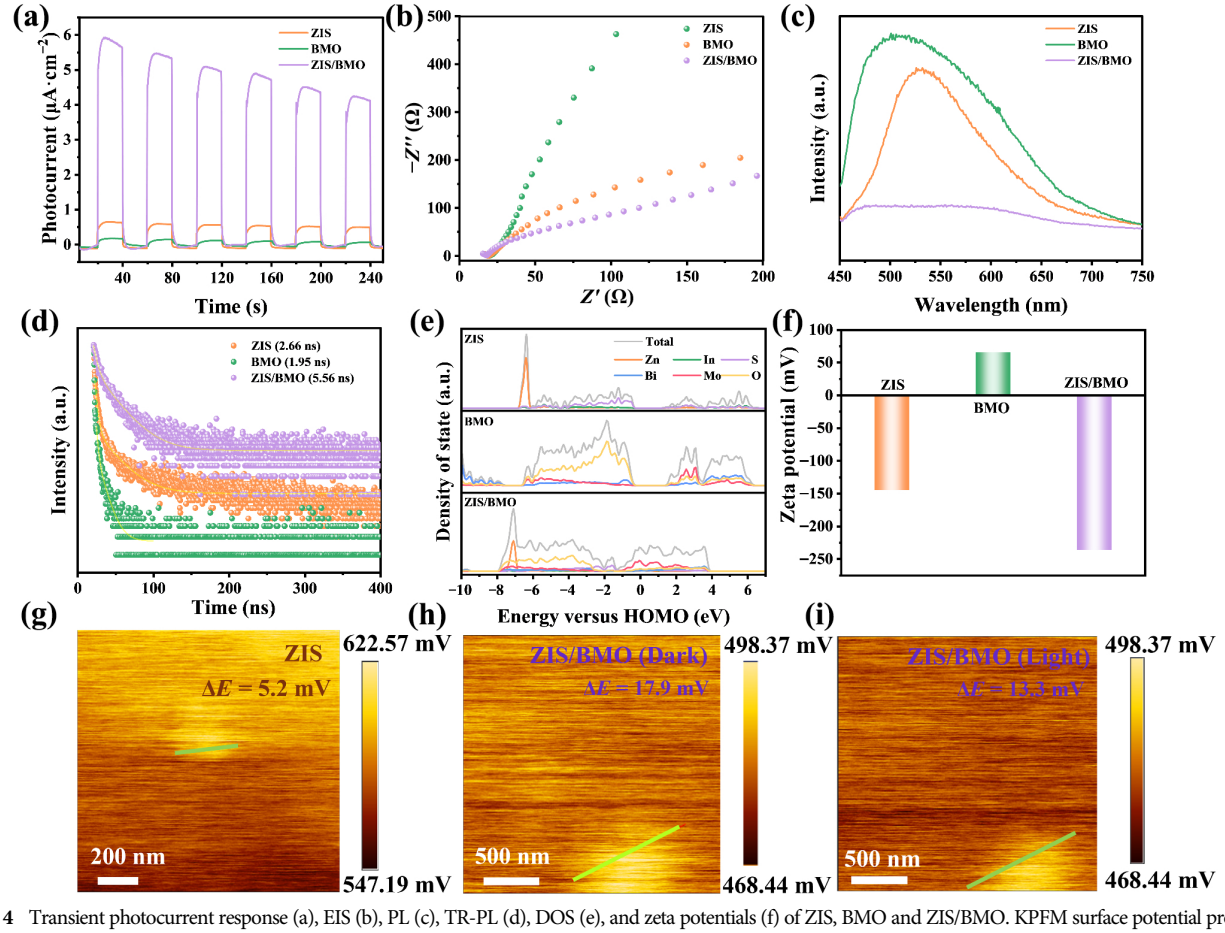


Figure 4 Transient photocurrent response (a), EIS (b), PL (c), TR-PL (d), DOS (e), and zeta potentials (f) of ZIS, BMO and ZIS/BMO. KPFM surface potential profiles of ZIS (g), ZIS/BMO in the dark (h) and under light (i).

enhancing the catalytic performance [62, 63]. To further explore the effect of BMO introduction on the IEF strength, the surface potential difference of ZIS and ZIS/BMO was investigated using Kelvin probe force microscopy (KPFM). As depicted in Figs. 4(g) and 4(h), ZIS exhibits a surface electrostatic potential of 5.2 mV. The surface electrostatic potential of the ZIS/BMO material is enhanced to 17.9 mV (Figs. S18(a) and S18(b) in the ESM). The enhancement in surface electrostatic potential indicates that the interfacial coupling between ZIS and BMO forms a stronger IEF, which promotes charge separation and transfer [64]. It is noteworthy that under illumination, the surface potential of the ZIS/BMO decreases to 13.3 mV (Fig. 4(i) and Fig. S18(c) in the ESM), yet this value remains significantly higher than that of the individual ZIS component. This is because the electric field generated by the depletion of dipoles due to the back-migrated photogenerated charges provides a strong driving force for charge migration to the surface, further confirming the charge transfer mechanism of this S-scheme heterojunction [65–67]. Fundamentally, the enhanced photocatalytic H_2O_2 production activity of ZIS/BMO originates from the synergistic effects of broadened light absorption, the established S-scheme heterojunction band alignment, an intensified IEF, and optimized interfacial charge dynamics, which collectively promote efficient photogenerated carrier separation and transport.

Rotating disk electrode (RDE) measurements were conducted to further probe the electron transfer processes involved in photocatalytic H_2O_2 production. As presented in, linear sweep voltammetry (LSV) curves for ZIS and ZIS/BMO were recorded at various rotation speeds (Figs. 5(a) and 5(b)). The number of electrons transferred (n) during the ORR was determined by analyzing the data with the Koutecký–Levich equation. In comparison to ZIS (n = 1.54), the ZIS/BMO (n = 2.03) exhibits an electron transfer number closer to 2, indicating a dominant $2e^-$ ORR pathway (Fig. 5(c)). In order to further clarify the reaction mechanism, electron paramagnetic resonance (EPR) spectroscopy was employed to identify the relevant reactive intermediates. As shown in Fig. 5(d), using DMPO as a spin-trapping agent, the $\cdot O_2^-$

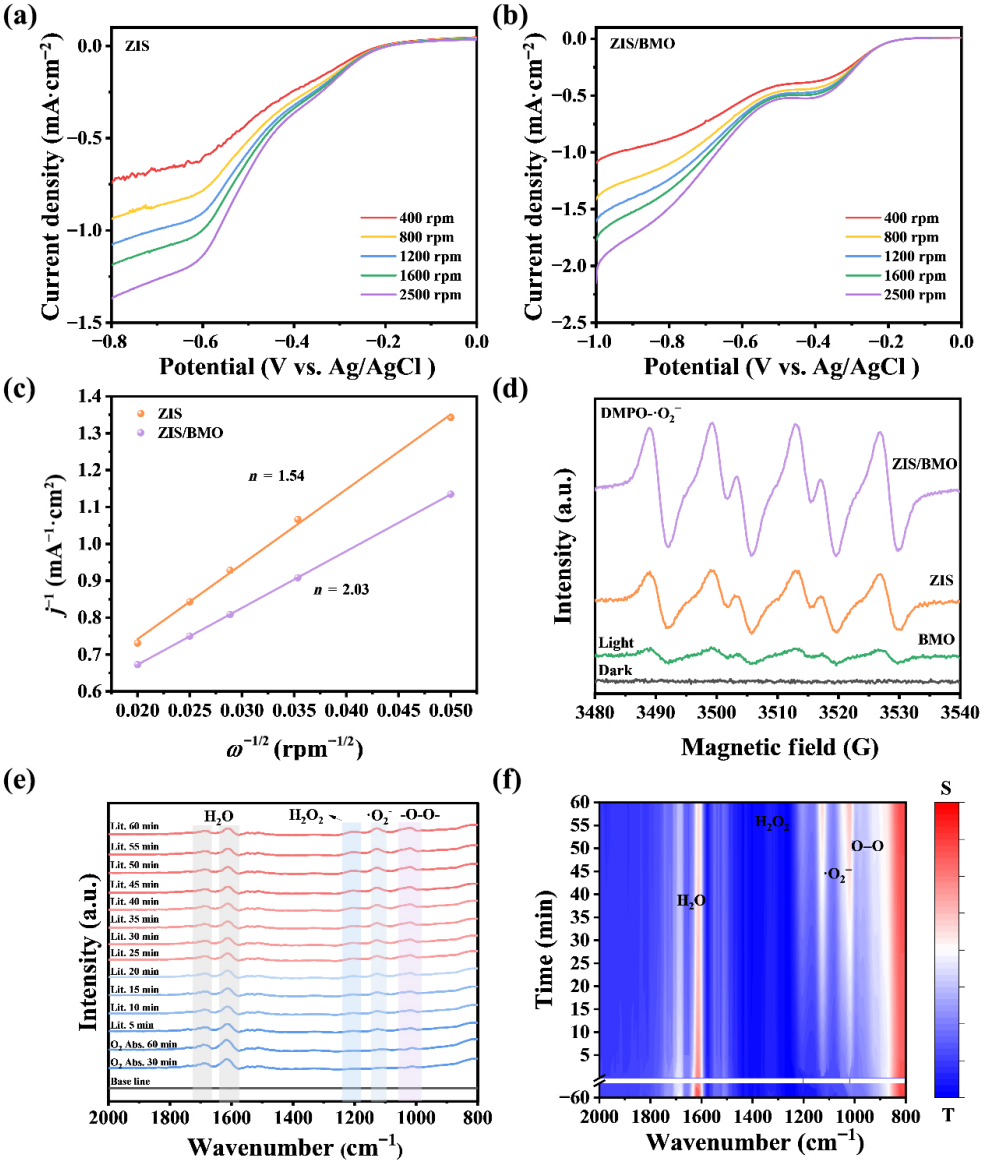


Figure 5 LSV curves (a) and (b) at different rotation speeds, the calculated average number of transferred electrons (c) and ESR signals for DMPO-superoxide radical (d) of ZIS and ZIS/BMO, *in-situ* DRIFT spectra of ZIS/BMO (e) and (f).

signal is observed only after light irradiation, demonstrating that light is a prerequisite for the generation of active species. Furthermore, the signal intensity for ZIS/BMO is significantly stronger than that for pure ZIS, indicating that the introduction of BMO promotes the separation of electron-hole pairs, which is more conducive to the ORR. After photoactivation, ·OH signals were detected in all the prepared materials, which is attributed to the decomposition of H_2O_2 under light (Fig. S19 in the ESM) [68]. This result indicates that the introduction of BMO is more favorable for the generation of H_2O_2 through the $2e^-$ ORR pathway. *In-situ* diffuse reflectance infrared Fourier transform spectroscopy (DRIFTS) was employed to identify the reactive intermediates formed during the photocatalytic reaction, with the results presented in Figs. 5(e) and 5(f). With prolonged light irradiation, the characteristic signals at 1016 cm^{-1} (assigned to O–O bond vibration), 1125 cm^{-1} (attributed to the superoxide radical, $\cdot O_2^-$), and 1206 cm^{-1} (associated with H_2O_2) were all observed to intensify significantly (Fig. S20 in the ESM). These findings provide further support for the mechanism that hydrogen peroxide is generated via a two-step single-electron ORR pathway [69].

4 Conclusion

In this study, an S-scheme ZIS/BMO heterojunction featuring Mo–S bonds as interfacial bridging linkages was successfully constructed for efficient photocatalytic H_2O_2 production, achieving a high generation rate of 1387 $\mu mol \cdot g^{-1} \cdot h^{-1}$ under visible light. Combined experimental characterizations and DFT calculations consistently reveal that the markedly improved activity arises from the synergy within the ZIS/BMO S-scheme heterojunction established through Mo–S interfacial bonds. This S-scheme heterojunction effectively broadens the light absorption range and optimizes the band structure, while the formation of Mo–S interfacial bonds provides an efficient interfacial transport pathway for photogenerated charge carriers. Together with the built-in electric field, it synergistically drives the spatial separation and directional migration of carriers, thereby preserving superior redox capability and enabling the efficient conversion of oxygen to H_2O_2 via a two-step single-electron oxygen reduction pathway. This study provides a feasible interfacial engineering strategy and mechanistic insights for designing efficient and stable S-scheme photocatalysts toward sustainable H_2O_2 synthesis.

Electronic Supplementary Material: Supplementary material (experimental procedures, detailed SEM and EDS images, XRD and FT-IR spectra, XPS spectra, electrochemical test results, theoretical calculation methods, tables, etc.) is available in the online version of this article at https://doi.org/10.26599/NR.2026.94908930.

Data availability

All data needed to support the conclusions in the paper are presented in the manuscript and the Electronic Supplementary Materials. Additional data related to this paper may be requested from the corresponding author upon request.

Acknowledgements

This work is supported by the Natural Science Foundation Project of Jilin Province (No. YDZJ202601ZYTS217) and the National Natural Science Foundation of China (No. 22478150).

Declaration of competing interest

The authors declare no conflicting interests regarding the content of this article.

Author contribution statement

C. B. L. conceived the idea for this review. S. Z. and T. S. drafted the manuscript. H. L. and G. Q. W. carried out the validation and visualization work. R. Q. G. and W. S. conducted data search and verification. X. Y. C. and X. J. Z. polished the language of the manuscript. Finally, all authors revised the manuscript.

Use of AI statement

None.

References

[1] Ren, P.; Liu, Y. M.; Nisar, I.; Das, S. Turning sunlight and seawater into energy: Photocatalytic hydrogen peroxide as a green fuel carrier. *Adv. Mater.* **2026**, *38*, e72660.

[2] Zhou, X. Y.; Cao, K. H.; Huang, S. Q.; Wu, H. N.; Cao, Z.; Liu, H.; Chen, P.; Su, D. W.; Wang, G. X.; Wang, T. Y. et al. Synergistic conversion of hydrogen peroxide and benzaldehyde in air by silver single-atom modified thiophene-functionalized g-C_3N_4. *Angew. Chem., Int. Ed.* **2025**, *64*, e202505532.

[3] Luan, T. X.; Wei, Q. L.; Xin, C. L.; Wong, S. Y.; Li, Y. H.; Zheng, Y. S.; Li, Y.; Liu, G. L.; Yu, W. W.; Loh, X. J. et al. Remarkably enhancing H_2O_2 photogeneration by modulating pore-microenvironment of a photoactive covalent organic framework. *Adv. Mater.* **2026**, *38*, e15517.

[4] Chen, Z.; Weng, H.; Chu, C. C.; Yao, D. C.; Li, Q. J.; Zhang, C.; Mao, S. Nitrogen heterocyclic covalent organic frameworks for efficient H_2O_2 photosynthesis and *in situ* water treatment. *Nat. Commun.* **2025**, *16*, 6943.

[5] Xi, D. W.; Wu, Y. H.; Li, Y. L.; Yan, Z. F.; Liu, R. Y.; Aziz, M. J. Electrifying industrial hydrogen peroxide production via soft interfacial molecular mediation. *Nat. Chem.* **2025**, *17*, 1883–1890.

[6] Zhang, Y.; Lewis, R. J.; Li, Z. C.; He, X. H.; Ji, H. B.; Hutchings, G. J. Direct synthesis of H_2O_2 by spatially separate hydrogen and oxygen activation sites on tailored Pt-Au catalysts. *Angew. Chem., Int. Ed.* **2026**, *65*, e21118.

[7] Li, Y. J.; Xu, J. Y.; Wang, S. Y.; Han, B.; Li, W. T.; Zhu, X. L.; Zhu, Y. F. Efficient surface reaction pathways in metal-free organic semiconductors for practical photocatalytic hydrogen peroxide production. *Sci. Bull.* **2025**, *70*, 2836–2851.

[8] Liu, Q.; Bi, H.; Zhao, R.; Yang, X. W.; Chen, F. Y.; Shen, Z. R. Fully exposed silver clusters enabling highly efficient photocatalytic H_2O_2 production in pure water. *Angew. Chem., Int. Ed.* **2025**, *64*, e202511687.

[9] Li, H.; Wang, W.; Xu, K. Q.; Cheng, B.; Xu, J. S.; Cao, S. W. Solar-driven H_2O_2 production by S-scheme heterojunction photocatalyst. *Chin. J. Catal.* **2025**, *72*, 24–47.

[10] Ruan, X. W.; Xu, M. H.; Zhang, X. L.; Ding, C. S.; Meng, D. P.; Leng, J.; Zhang, W.; Ravi, S. K.; Cui, X. Q. Dual plasmonic fields enable high-density hot-electron generation with stepwise charge transfer directed to oxygen reduction sites for enhanced artificial photosynthesis of H_2O_2. *Adv. Energy Mater.* **2025**, *15*, 2502302.

[11] Dang, X. M.; Wu, S.; Gan, X. R.; Zhang, H. G.; Jiang, X.; Zhang, Y. B.; Zhao, H. M. Dual-channels heterojunction interface engineering for efficient hydrogen peroxide photoproduction. *Adv. Funct. Mater.* **2026**, *36*, e74965.

[12] Miao, Y. Y.; Yuan, J. L.; Zhou, L.; Ding, X.; Yang, Y.; Wang, S. Y.; Zhang, X. H.; Chen, H.; Chen, F. S. Enhancing hydrogen production

from photocatalytic water splitting over $ZnIn_2S_4$/Ni-MOF via magnetically induced spin polarization. *Appl. Catal. B: Environ. Energy* **2026**, *387*, 126513.

[13] Ruan, X. W.; Ding, C. S.; Leng, J.; Jiao, D. X.; Zhang, X. X.; Xu, M. H.; Meng, D. P.; Cui, X. Q.; Zheng, Z. K.; Zhu, Y. F. et al. Decoupling of carrier pathways in Au/Cu-$Zn_3In_2S_6$ through bulk hole trapping and surface hot electron accumulation enhances photocatalytic hydrogen peroxide production. *Adv. Mater.* **2025**, *37*, e11422.

[14] Jiang, Q.; Shang, Q.; Li, J. M.; Zhao, L.; Liang, Z. H.; Wang, G. H.; Peng, X. K.; Wang, J. Dual internal electric field-modulated Sv-$ZnIn_2S_4$/$BaTiO_3$ heterojunction for enhanced piezo-photocatalytic performance. *Appl. Surf. Sci.* **2026**, *720*, 165159.

[15] Qiao, X. Q.; Guo, H.; Du, P. C.; Sun, B. J.; Hou, D. F.; Wang, M. D.; Wu, X. Q.; Huang, S. C.; Sun, C. H.; Wu, T. et al. Dual-vacancy enhanced built-in electric field boosting plasmonic S-scheme photocatalysis for superior hydrogen evolution. *J. Energy Chem.* **2026**, *113*, 1–11.

[16] Xue, S.; Wei, S.; Guo, B. Q.; Cui, J. F.; Zhao, Z. M.; Li, G. C.; Wang, L.; Huang, J. F.; Meng, A. L.; Wang, X. H. et al. Unlock high-efficiency $ZnIn_2S_4$ photocatalysis via designing hierarchical cocatalyst: Synergistic modulation of interfacial charge transfer and hydrogen adsorption. *Appl. Catal. B: Environ. Energy* **2026**, *385*, 126315.

[17] Yang, J.; Xie, T. P.; Mei, Y. H.; Chen, J. Y.; Sun, H.; Feng, S.; Zhang, Y.; Zhao, Y.; Wang, J. K.; Li, X. Q. et al. High-efficiency V-mediated Bi_2MoO_6 photocatalyst for PMS activation: Modulation of energy band structure and enhancement of surface reaction. *Appl. Catal. B: Environ.* **2023**, *339*, 123149.

[18] Lin, J.; He, J. L.; Huang, Q. L.; Luo, Y.; Zhang, Y.; Li, W.; Zhou, G. B.; Hu, J. Q.; Yang, Z.; Zhou, Y. Interfacial Bi–O–C bonds and rich oxygen vacancies synergistically endow carbon quantum Dot/Bi_2MoO_6 with prominent photocatalytic CO_2 reduction into CO. *Appl. Catal. B: Environ. Energy* **2025**, *362*, 124747.

[19] Chen, H. J.; Xu, R. H.; Chen, D.; Lu, T. L.; Li, H. J.; Wang, M. Subsurface Mo vacancy in bismuth molybdate promotes photocatalytic oxidation of lactate to pyruvate. *ACS Catal.* **2024**, *14*, 1977–1986.

[20] Tai, R.; Xu, W. L.; Sui, X.; Liu, X. R.; Wang, C. Z.; Wang, Q. Efficient adsorption and mechanism analysis of antibiotics by UiO-66-NH_2/Bi_2MoO_6 composite materials. *Sep. Purif. Technol.* **2025**, *360*, 130818.

[21] Han, Y. S.; Ling, W. K.; Dai, Y.; Chen, T. T.; Li, J. M.; Ma, J. L.; Sun, R. C. Charge-directed hole enrichment via nitrogen defect-coupled S-scheme heterojunction for efficient selective oxidation of xylose/xylan to co-produce chemicals and fuels. *Appl. Catal. B: Environ. Energy* **2026**, *389*, 126595.

[22] Wu, X. H.; Sayed, M.; Wang, G. H.; Yu, W. L.; Zhu, B. C. COF-based S-scheme heterojunction photocatalyst. *Adv. Mater.* **2026**, *38*, e11322.

[23] Wu, J. X.; Qiao, P. Z.; An, P.; Zhang, M. S.; Xiu, H.; Song, Z. Y.; Li, K. D.; Cui, Y. P.; Wang, Y. J.; Yao, W. Q. Modulating interfacial Mo–S chemical-bond enable highly-efficient charge transfer for promoted visible-light-driven photocatalytic hydrogen evolution. *Appl. Catal. B: Environ. Energy* **2025**, *377*, 125481.

[24] Wang, B. F.; Wang, H. W.; Xu, W. Y.; Chang, Z. L.; Li, J. L.; Gong, Y. T.; Huang, F.; Wang, J. J.; Li, X. L. Boosting photocatalytic hydrogen production in complex environments by confining trace $MoBT_x$ MBene. *Sci. Adv.* **2026**, *12*, eaed6189.

[25] Wang, C. H.; Li, Y.; Fan, M. H.; Yu, X.; Ding, J.; Yan, L.; Qin, G.; Yang, J.; Zhang, Y. C. Controllable growth of silver nanoparticles on titanium dioxide/nitrogen-doped carbon nanofiber/molybdenum disulfide: Toward enhanced photocatalytic-activating peroxymonosulfate performance and "memory catalysis". *Chem. Eng. J.* **2024**, *479*, 147752.

[26] Xu, Q. L.; Wageh, S.; Al-Ghamdi, A. A.; Li, X. Design principle of S-scheme heterojunction photocatalyst. *J. Mater. Sci. Technol.* **2022**, *124*, 171–173.

[27] Ji, Y. X.; Luan, G. Q.; Wei, J. Y.; Bao, L. Q.; Cui, M. Y.; Tian, Z. H.; Li, C. H. Zinc indium sulfide coupling with graphitic carbon nitride containing non-intrinsic oxygen vacancies to form Z-scheme heterojunction for boosting photodegradation of tetracycline. *J. Environ. Chem. Eng.* **2024**, *12*, 113938.

[28] Xu, Z. D.; Sun, T.; Li, Z. X.; Yu, F.; Bai, H.; Qi, Y. F.; Guan, R. Q.; Liu, C. B. Effective killing of multidrug resistant bacteria by Bi_2MoO_6 nanospheres rich in oxygen vacancy under visible light. *Sep. Purif. Technol.* **2025**, *354*, 129085.

[29] Gao, C. M.; Xie, Y.; Chen, Y.; Ling, Y.; Ma, Y. C.; Zhang, Y. F.; Shao, Y. Construction of $ZnIn_2S_4$/Bi_2MoO_6 heterojunction enhancement photocatalytic hydrogen evolution performance under visible light. *Int. J. Hydrogen Energy* **2024**, *52*, 90–99.

[30] Peng, H. P.; Yang, H. C.; Han, J. J.; Liu, X. Z.; Su, D.; Yang, T.; Liu, S. H.; Pao, C. W.; Hu, Z. W.; Zhang, Q. B. et al. Defective $ZnIn_2S_4$ nanosheets for visible-light and sacrificial-agent-free H_2O_2 photosynthesis via O_2/H_2O redox. *J. Am. Chem. Soc.* **2023**, *145*, 27757–27766.

[31] Wei, Y.; Wu, Y. Z.; Wang, J.; Wu, Y. H.; Weng, Z. L.; Huang, W. Y.; Yang, K.; Zhang, J. L.; Li, Q.; Lu, K. Q. et al. Rationally designed dual cocatalysts on $ZnIn_2S_4$ nanoflowers for photoredox coupling of benzyl alcohol oxidation with H_2 evolution. *J. Mater. Chem. A* **2024**, *12*, 18986–18992.

[32] Ma, T. X.; Yang, C. M.; Guo, L.; Soomro, R. A.; Wang, D. J.; Xu, B.; Fu, F. Refining electronic properties of Bi_2MoO_6 by in-doping for boosting overall nitrogen fixation via relay catalysis. *Appl. Catal. B: Environ.* **2023**, *330*, 122643.

[33] Geng, L.; Li, W. J.; Liu, X. T.; Li, X. Y.; Fan, H. X.; Qiu, H.; Ma, X. H.; Dong, M. Active sites modification and superior carriers separation synergistically boosted hydrogen production of Bi/Bi_2MoO_6/$ZnIn_2S_4$ non-noble metal S-scheme photocatalyst. *J. Colloid Interface Sci.* **2023**, *629*, 723–732.

[34] Yang, M.; Zhan, X. Q.; Ou, D. L.; Wang, L.; Zhao, L. L.; Yang, H. L.; Liao, Z. Y.; Yang, W. Y.; Ma, G. Z.; Hou, H. L. Efficient visible-light-driven hydrogen production with ag-doped flower-like $ZnIn_2S_4$ microspheres. *Rare Met.* **2025**, *44*, 1024–1041.

[35] Xue, J. Q.; Xiao, W.; Shi, L.; Liu, Y. J.; Wang, P.; Bi, Q. Efficient degradation of ciprofloxacin by a flower-spherical Bi_2MoO_6/BiOCl Z-type heterojunction photocatalyst enriched with oxygen vacancies. *J. Environ. Chem. Eng.* **2023**, *11*, 111235.

[36] He, J. L.; Lin, J.; Zhang, Y.; Hu, Y. F.; Huang, Q. L.; Zhou, G. B.; Li, W.; Hu, J. Q.; Hu, N.; Yang, Z. Interfacial Mo–S bond-reinforced hierarchical S-scheme heterostructure of Bi_2MoO_6@$ZnIn_2S_4$ for highly-selective and efficient CO_2 photoreduction into CO. *Chem. Eng. J.* **2024**, *480*, 148036.

[37] Ma, T. X.; Li, R. Q.; Huang, Y. C.; Lu, Y. X.; Guo, L.; Niu, M. M.; Huang, X.; Soomro, R. A.; Ren, J. Y.; Wang, Q. et al. Interfacial chemical-bonded MoS_2/In-Bi_2MoO_6 heterostructure for enhanced photocatalytic nitrogen-to-ammonia conversion. *ACS Catal.* **2024**, *14*, 6292–6304.

[38] Yang, X.; Jin, Y. C.; Ke, S. Z.; Li, M. Q.; Yang, X. H.; Shen, L. J.; Yang, M. Q. Cooperative S–S coupling and H_2 production from photocatalytic dehydrogenation of thiols over $ReSe_2$/$ZnIn_2S_4$ heterostructure. *Chem. Eng. J.* **2024**, *499*, 155687.

[39] Xiong, R. Z.; Ke, X. X.; Jia, W. F.; Xiao, Y. H.; Cheng, B. C.; Lei, S. J. Photothermal-coupled solar photocatalytic CO_2 reduction with high efficiency and selectivity on a MoO_{3-x}@$ZnIn_2S_4$ core–shell S-scheme heterojunction. *J. Mater. Chem. A* **2023**, *11*, 2178–2190.

[40] Wei, S. T.; Yang, D.; Guan, R. Q.; Xu, P.; Wang, Y. X.; Teng, Y. M.; Li, A. C.; Zhang, J. K.; Tan, H. Q.; Wang, L. et al. High pressure torsion technology applied to ZnO nanomaterials for enhancing the room-temperature HCl sensing performance. *Chem. Eng. J.* **2025**, *525*, 170238.

[41] Wu, Y.; Yang, Y.; Gu, M. L.; Bie, C. B.; Tan, H. Y.; Cheng, B.; Xu, J.

S. 1D/0D heterostructured $ZnIn_2S_4$@ZnO S-scheme photocatalysts for improved H_2O_2 preparation. *Chin. J. Catal.* **2023**, *53*, 123–133.
[42] Ruan, X. W.; Ding, C. S.; Jiao, D. X.; Leng, J.; Xu, M. H.; Li, B. N.; Yu, Z. P.; Cui, X. Q.; Yu, J. C.; Zhu, Y. F. et al. Ga-on-in substitution with Zn vacancies in $Zn_3In_2S_6$ induces electron-hole asymmetry and in-O bond weakening for coupled two-electron oxygen reduction and H_2O_2 stabilization. *Adv. Mater.* **2026**, *38*, e22831.
[43] Fan, H.; Ai, L. L.; Xu, M. J.; Wu, S. M.; Wang, L. X.; Tan, C. A novel dual-channel $ZnIn_2S_4/Bi_4Ti_3O_{12}$ S heterojunction significantly enhances photocatalytic hydrogen peroxide synthesis. *J. Colloid Interface Sci.* **2025**, *697*, 137896.
[44] Chen, C.; Du, S. W.; Wang, Y. M.; Han, Z. W.; Zhang, S. Y.; Ma, W. M.; Xu, H.; Fang, P. F. Hollow $MoSe_2$/N-doped carbon composited with $ZnIn_2S_4$ constructing dual Z-scheme heterojunction for enhanced visible-light photocatalytic performances. *J. Colloid Interface Sci.* **2026**, *701*, 138758.
[45] Wang, D. D.; Lin, Z. X.; Yang, W. T.; Li, H. J.; Su, Z. M. $Bi_2MoO_6/MgIn_2S_4$ S-scheme heterojunction with rich oxygen vacancies for effective organic pollutants degradation: Degradation pathways, biological toxicity assessment, and mechanism research. *J. Solid State Chem.* **2025**, *341*, 125054.
[46] Wang, D. D.; Lin, Z. X.; Yang, W. T.; Li, H. J.; Su, Z. M. $Bi_2MoO_6/ZnIn_2S_4$ S-scheme heterojunction containing oxygen vacancies for photocatalytic degradation of organic pollutant. *J. Mol. Struct.* **2025**, *1321*, 139914.
[47] Xiong, S. F.; Liu, X. N.; Shen, Z. G.; Hu, Z. T.; Yang, H. Y.; Hao, J.; Cai, J. J.; Yang, J. Selective oxidation of 5-hydroxymethyl furfural coupled with H_2 production over surface sulfur vacancy-rich $Zn_3In_2S_6/Bi_2MoO_6$ heterojunction photocatalyst. *Inorg. Chem.* **2023**, *62*, 20120–20128.
[48] Gu, H. J.; Zhang, H. H.; Wang, X. L.; Li, Q.; Chang, S. Y.; Huang, Y. M.; Gao, L. L.; Cui, Y. Y.; Liu, R. W.; Dai, W. L. Robust construction of CdSe nanorods@Ti_3C_2 MXene nanosheet for superior photocatalytic H_2 evolution. *Appl. Catal. B: Environ.* **2023**, *328*, 122537.
[49] Qian, G. L.; Li, J. X.; Tan, H. L.; Tang, L. Y.; Yu, X. L.; Li, W. T.; Ma, S. H.; Xie, Q.; Li, J.; Long, D. *In-situ* fabrication of oxygen vacancy rich S-scheme Bi_2MoO_6/MoS_xSe_y heterojunction for efficient CO_2 photoreduction with low-concentration. *Appl. Catal. B: Environ. Energy* **2026**, *383*, 126017.
[50] Jiang, X.; Fan, D.; Yao, X. T.; Dong, Z. Y.; Li, X. Y.; Ma, S. S.; Liu, J. C.; Zhang, D. F.; Li, H. S.; Pu, X. P. et al. Highly efficient flower-like $ZnIn_2S_4/CoFe_2O_4$ photocatalyst with p-n type heterojunction for enhanced hydrogen evolution under visible light irradiation. *J. Colloid Interface Sci.* **2023**, *641*, 26–35.
[51] Liang, Q.; Fan, J. S,; Deng, X. Z.; Liu, J. C.; Zeng, J. R.; Zhang, H.; Li, J.; Liu, C. H.; Kang, Z. H.; Zhao, Z. Oxygen vacancy-driven asymmetrical charge distribution on Bi-O-Sn sites in Sn-doped Bi_2MoO_6 for efficient photocatalytic CO_2-to-CH_4 conversion. *Angew. Chem., Int. Ed.* **2026,** *65*, e21874.
[52] Sun, T.; Deng, Y. H.; Wang, G. Q.; Yan, L.; Sun, T. T.; Guan, R. Q.; Zhang, S. W.; Liu, C. B. Charge carrier controlled free radical construction efficient photocatalytic self-fenton system. *Chem. Eng. J.* **2024**, *496*, 154351.
[53] Xu, L. P.; Li, L. J.; Hu, Z. F.; Yu, J. C. EDTA-enhanced photocatalytic oxygen reduction on K-doped g-C_3N_4 with N-vacancies for efficient non-sacrificial H_2O_2 synthesis. *J. Catal.* **2023**, *418*, 300–311.
[54] Tang, W. Y.; Li, Z. W.; Shi, X. R.; Zhang, D. X.; Jin, D. F.; Li, Y. Q.; Fan, H. T.; Li, B.; Wang, L. Y.; Hou, J. G. Sacrificial-free H_2O_2 photosynthesis on organic-inorganic core–shell heterojunction under visible light irradiation. *J. Colloid Interface Sci.* **2025**, *694*, 137670.
[55] Guo, Y.; Tong, X. L.; Yang, N. J. Photocatalytic and electrocatalytic generation of hydrogen peroxide: Principles, catalyst design and performance. *Nano-Micro Lett.* **2023**, *15*, 77.
[56] Xu, S. Q.; Chen, K. Y.; Cai, Y. Q.; Ren, S. X.; Chu, W. H.; Song, M.; Xu, Y. M.; Tan, C. Q. Unveiling the neglected role of alcohols and phenolic compounds in photocatalysis H_2O_2 generation chemistry. *Water Res.* **2025**, *285*, 124139.
[57] Mou, Y.; Wu, X. D.; Qin, C. C.; Chen, J. Y.; Zhao, Y. L.; Jiang, L. B.; Zhang, C.; Yuan, X. Z.; Huixiang Ang, E.; Wang, H. Linkage microenvironment of azoles-related covalent organic frameworks precisely regulates photocatalytic generation of hydrogen peroxide. *Angew. Chem., Int. Ed.* **2023**, *62*, e202309480.
[58] Yu, Z. W.; Yu, F. T.; Xu, M.; Feng, S. F.; Qiu, J. D.; Hua, J. L. Amidoxime-functionalized sp^2-carbon-conjugated covalent organic frameworks for overall photocatalytic hydrogen peroxide production. *Adv. Sci.* **2025**, *12*, 2415194.
[59] Ma, L. Y.; Hu, J. P.; Deng, C. J.; Mei, P.; Han, X. Y.; Ba, H. C.; Li, Z. H.; Zhang, D. H.; Huang, S. Z. Promoting the potassium storage of 2D layered indium sulfide through zinc incorporation and MXene coupling. *Adv. Funct. Mater.* **2025**, *35*, 2418733.
[60] Jian, L.; Dong, Y. M.; Zhao, H.; Pan, C. S.; Wang, G. L.; Zhu, Y. F. Highly crystalline carbon nitrogen polymer with a strong built-in electric fields for ultra-high photocatalytic H_2O_2 production. *Appl. Catal. B: Environ.* **2024**, *342*, 123340.
[61] Yang, J. H.; Ma, B. J.; Zhu, Y. F. A novel NDI/PTA organic heterojunction photocatalyst with built-in electric field for efficient hydrogen production. *Appl. Catal. B: Environ. Energy* **2026**, *381*, 125890.
[62] Qi, Y. Y.; Li, S. M.; Bao, T. F.; She, P.; Rao, H.; Qin, J. S. Flower-like Z-scheme heterostructure of cobalt porphyrin/$ZnIn_2S_4$ for boosting photocatalytic solar fuel production. *Appl. Catal. B: Environ. Energy* **2024**, *357*, 124299.
[63] Liu, X.; Yuan, M.; Li, Y. D.; Sun, B. W.; Yang, X. H.; Su, Y. C.; Luo, J. H. Te^{2-} modulated heterogeneous remodeling of S Atoms in ultrathin $ZnIn_2S_4$ nanosheets containing S vacancies synergistically enhances CO_2 photoreduction. *J. Colloid Interface Sci.* **2025**, *679*, 772–784.
[64] Li, L. Y.; Lv, X. M.; Xue, Y. Y.; Shao, H. B.; Zheng, G. F.; Han, Q. Custom-design of strong electron/proton extractor on COFs for efficient photocatalytic H_2O_2 production. *Angew. Chem., Int. Ed.* **2024**, *63*, e202320218.
[65] Xu, Q. L.; Zhang, L. Y.; Cheng, B.; Fan, J. J.; Yu, J. G. S-scheme heterojunction photocatalyst. *Chem* **2020**, *6*, 1543–1559.
[66] Xu, M. L.; Lu, M.; Qin, G. Y.; Wu, X. M.; Yu, T.; Zhang, L. N.; Li, K.; Cheng, X.; Lan, Y. Q. Piezo-photocatalytic synergy in $BiFeO_3$@COF Z-scheme heterostructures for high-efficiency overall water splitting. *Angew. Chem., Int. Ed.* **2022**, *61*, e202210700.
[67] Deng, X. X.; Chen, P.; Cui, R. R.; Gong, X. Y.; Li, X. C.; Wang, X.; Deng, C. Y. Local charge rectification and electronic interactions in $ZnIn_2S_{4-x}$-Bi_2MoO_{6-x} heterojunction for enhancing synergistic piezo-photocatalytic hydrogen evolution and benzylamine oxidation. *Nano Energy* **2024**, *126*, 109657.
[68] Sun, T.; Deng, Y. H.; Wang, G. Q.; Liu, H.; Chen, L.; Guan, R. Q.; Liu, C. B.; Che, G. B.; Cheng, X. Y.; Zhu, Y. F. Nb_2C-induced local electron enrichment drives O_2 activation and *OOH stabilization for efficient photocatalytic H_2O_2 synthesis. *Appl. Catal. B: Environ. Energy* **2026**, *382*, 125907.
[69] Cao, D.; Du, J. C.; Li, J. G.; Sun, Q.; Guan, J.; Liu, J. T. Hydroxyl-functionalized donor-acceptor covalent organic frameworks for efficient photocatalytic hydrogen peroxide production under visible light. *ACS Catal.* **2025**, *15*, 3584–3594.

This is an open access article under the terms of the Creative Commons Attribution 4.0 International License (CC BY 4.0, https://creativecommons.org/licenses/by/4.0/).

© The Author(s) 2026. Published by Tsinghua University Press.